Autonomous Transition Flight for a Vertical Take-Off and Landing Aircraft

Pedro Casau

***Abstract*— This paper addresses modelling and control problems for an model-scale Unmanned Air Vehicle (UAV) which is intended to perform Vertical Take-Off and Landing (VTOL) autonomously as well as transition to level flight. The first contribution of this thesis is the description of an accurate UAV nonlinear model which captures both hovering and level flight behaviors. Furthermore, the Hybrid Automata framework is introduced into the model by means of *supervisory control* which provides dynamics switching between modes of operation. The second contribution concerns the problems of *i)* hover and level flight stabilization and, *ii)* Transition trajectory tracking by means of linear control techniques. Finally, a control law which renders the system locally Input-to-State Stable (ISS) is designed within the Hybrid Systems' framework allowing for practical trajectory tracking.**

I. INTRODUCTION

The demand for Unmanned Air Vehicles (UAVs) has escalated in the past few years due to their contributions in commercial and defense applications, including fire surveillance and mitigation operations, agricultural fields spraying, infrastructure inspection, among others (see e.g. [1] and [2]). Several UAV configurations have been developed to meet the requirements imposed by such applications, including fixed-wing and tilt wing aircraft, rotorcrafts and ducted-fan vehicles.

Recent developments described in [3] have shown that fixed-wing Vertical Take-Off and Landing (VTOL) aircrafts can perform both long endurance missions and precise maneuvering within exiguous environments. The versatility of such aircrafts combines helicopter precise trajectory tracking with conventional fixed-wing airplanes ability to cover large distances, delivering a final solution which largely exceeds the capabilities of its predecessors. However, the problem of achieving robust transitions between hover and leveled flights is difficult for its exquisite dynamics. To this end, several control methodologies have been employed, including robust linear control, feedback linearization techniques and adaptive controllers (see e.g. [4] and [5]) but these different approaches still lack a formal proof of stability and robustness.

The very different aircraft dynamics between hover and leveled flights suggest that supervisory control (i.e. the application of different control techniques for each operating mode) is a plausible solution for the given problem. Similar methodologies, like the ones described in [6] and [7], have been successfully employed in a variety of applications. Controller switching during operating mode transitions adds discrete behavior to the continuous UAV model, creating a new layer of complexity which must be dealt appropriately.

Systems which display both continuous and discrete behavior have been under an intense research effort over the last decade. This study has given rise to several concepts such as hybrid automata [8] and switched systems [9] which fall within the broader category of Hybrid Dynamical Systems described in [6]. The discrete behavior built into these systems may appear naturally for certain applications such as UAV landing and take-off (see e.g. [10]) but may also be the consequence of digital control or supervisory control [11].

The solution proposed in this thesis employs supervisory control by modeling the small-scale UAV within the Hybrid Automata framework, dividing the aircraft flight envelope into Hover, Transition and Level operating modes. Linear optimal control techniques are employed for system stabilization in hover and level flight while linear and nonlinear control solutions are exploited for stabilization during transition flight.

This paper is organized as follows. Section II presents the 3-dimensional UAV nonlinear model, explaining thoroughly the gravity, propeller and aerodynamic interactions with the aircraft body while the Hybrid Automaton introduced in Section III models the switching events introduced by supervisory control. Section IV presents the controller structures which are employed during local stabilization and the tracking of the reference trajectories. Finally, Section V presents the nonlinear controller structure which renders the closed-loop system Input-to-State Stable.

II. UAV NONLINEAR MODEL

The UAV under analysis is the model-scale fixed wing aircraft depicted in Figure 1a which has a total of six actuators: two propellers, the elevator, the rudder, the ailerons and the flaps. The UAV nonlinear model introduced in the following sections is described in the is represented by the differential equations $\dot{\boldsymbol{\xi}} = f(\boldsymbol{\xi}, \boldsymbol{\mu})$ with system state $\boldsymbol{\xi} \in \mathbb{R}^{14}$ and actuators input $\boldsymbol{\mu} \in \mathbb{R}^6$ given by

$$\boldsymbol{\xi} = [n_1\ n_2\ u\ v\ w\ p\ q\ r\ \phi\ \theta\ \psi\ x\ y\ z]^T \tag{1}$$

$$\boldsymbol{\mu} = [\tau_1\ \tau_2\ \delta_a\ \delta_e\ \delta_r\ \delta_f], \tag{2}$$

where $n_{1,2}$ is the propeller 1(2) speed, $\mathbf{v}_B = [u\ v\ w]^T$ is the aircraft linear velocity, $\boldsymbol{\omega}_B = [p\ q\ r]^T$ is the aircraft angular velocity, ϕ is the roll angle, θ is the pitch angle, ψ is the yaw angle, ${}^N\mathbf{p}_B = [x\ y\ z]^T$ is the aircraft position (in the North-East-Down reference frame), $\tau_{1,2}$ is the propeller 1(2) input torque, and δ_a, δ_e, δ_r and δ_f are the aileron, elevator, rudder and flap deflections, respectively.

The aircraft dynamic model includes not only the conventional six degree of freedom dynamics but also the propeller dynamics. The two inertial reference frames North-East-Down $\{N\}$ and Up-East-North $\{U\}$ are required in order to prevent parametrization singularities, provided that there

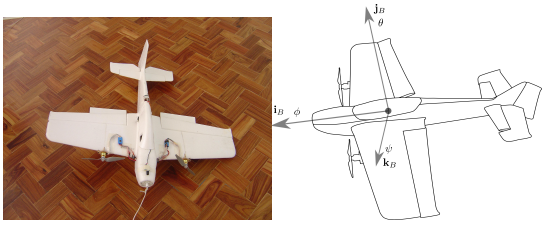

(a) Model-scale UAV picture (b) UAV model representation.

Fig. 1: The unmanned controlled vehicle.

exists appropriate switching between them. The North-East-Down reference frame $\{N\}$ is located at some point on the Earth's surface (which is assumed to be flat and still) and is defined by the set of unitary vectors $\{\mathbf{i}_N, \mathbf{j}_N, \mathbf{k}_N\}$ where: $\mathbf{i}_N$ is tangent to the earth's surface and points to the geographic North; $\mathbf{j}_N$ is normal to $\mathbf{i}_N$, tangent to the Earth's surface and points to the East; $\mathbf{k}_N$ completes the right handed set.

The Up-East-North reference frame $\{U\}$ origin is coincident with that of $\{N\}$ and is defined by the set of unitary vectors $\{\mathbf{i}_U, \mathbf{j}_U, \mathbf{k}_U\}$ where: $\mathbf{k}_U$ is tangent to the earth's surface and points to the geographic North; $\mathbf{j}_U$ is normal to $\mathbf{k}_U$, tangent to the Earth's surface and points to the East; $\mathbf{i}_U$ completes the right handed set.

The Body Reference Frame $\{B\}$ has its origin in the aircraft center of gravity and is defined orthogonal and right handed set of unitary vectors $\{\mathbf{i}_B, \mathbf{j}_B, \mathbf{k}_B\}$ which satisfy the following specifications: $\mathbf{i}_B$ is collinear with the aircraft's zero lift axis (roll axis); $\mathbf{j}_B$ is normal to the symmetry plane (pitch axis); $\mathbf{k}_B$ completes the right handed set (yaw axis). For the sake of simplicity, the Body Reference Frame is considered to be the principal axis of inertia.

The propellers, aerodynamic loads and gravity produce the forces and moments which affect the aircraft's behavior.

The gravity field produces a force which is directed towards the nadir and is given by

$$^{N}\mathbf{f}_g = [0\ 0\ mg]^T, \tag{3}$$

$$^{U}\mathbf{f}_g = [-mg\ 0\ 0]^T, \tag{4}$$

$$\mathbf{f}_g = {}^{B}_{I}\mathbf{R}^{I}\mathbf{f}_g, \tag{5}$$

in the reference frames $\{N\}$, $\{U\}$ and $\{B\}$, respectively. The gravity moment is null because the center of gravity (CG) is coincident with the center of mass (CM).

The propellers dynamics and thrust are mainly characterized by their Coefficient of Thrust C_T and Coefficient of Power C_P which are approximately given by

$$C_T = C_{T_0}\left(1 - \frac{J}{J_M}\right), \tag{6}$$

$$C_P = C_{P_0} + \left(\frac{J}{J_M}\right)^2 (C_{P_M} - C_{P_0}), \tag{7}$$

where $J = u/nd$ is the propeller advance ratio, n is the propeller's speed, d is the diameter, C_{T_0} is the Coefficient of Thrust at zero velocity, C_{P_0} is the Coefficient of Power at zero velocity, J_M is the advance ratio of zero thrust and C_{P_M} is the Coefficient of Power at $J = J_M$. C_T and C_P are related with the propeller's thrust and power according to

$$T = \rho n^2 d^4 C_T(J), \tag{8}$$

$$P = \rho n^3 d^5 C_P(J), \tag{9}$$

where ρ is the atmospheric density. The propeller's dynamic model is approximated by

$$I_p 2\pi\dot{n} = \tau - Q, \tag{10}$$

where I_p is its moment of inertia, τ is the input torque and Q is the aerodynamic drag torque acting on the propeller which is given by

$$Q = \frac{P}{2\pi n}. \tag{11}$$

The set of moments acting on the aircraft body due to propeller rotation ($\mathbf{m}_p$) includes the acceleration torque ($\mathbf{m}_{acc}$), the drag torque ($\mathbf{m}_{drag}$), the gyroscopic torque ($\mathbf{m}_{gyro}$) and the displacement torque ($\mathbf{m}_{dis}$) which arises from the displacement $\mathbf{r}_p$ of the propeller's center with respect to the center of gravity. These torques are given by

$$\mathbf{m}_{p_i} = \mathbf{m}_{acc_i} + \mathbf{m}_{drag_i} + \mathbf{m}_{gyro_i} + \mathbf{m}_{dis_i}, \tag{12}$$

$$\tag{13}$$

where subscript $i \in \{1, 2\}$ in the formulæ above distinguishes each propeller and their moments' sign change according to the propeller's rotation. The total thrust and torque produced by the propellers is given by

$$\mathbf{f}_p = \begin{bmatrix} T_{p_1} + T_{p_2} \\ 0 \\ 0 \end{bmatrix}, \tag{14}$$

$$\mathbf{m}_p = \mathbf{m}_{p_1} + \mathbf{m}_{p_2}. \tag{15}$$

The aerodynamic forces are generated from the propeller slipstream flow and the free-stream flow. The two contributions are calculated separately and combined together in the end using superposition. Under this assumption, the propeller slipstream velocity u_p is given by

$$u_p = \sqrt{\frac{8T}{\rho\pi d^2}}, \tag{16}$$

considering a steady, incompressible and inviscid flow.

The lifting surfaces' lift L_i and drag D_i is given by the following equations for any $u \geq 0$

$$L_i = \frac{1}{2}\rho A_i u_\infty^2 C_{L_i}, \tag{17}$$

$$D_i = \frac{1}{2}\rho A_i u_\infty^2 C_{D_i}, \tag{18}$$

where A_i is the surface's planform area and $u_\infty = u$ under the small angle approximation. These aerodynamic forces greatly depend on the surface's *Coefficient of Lift* (C_L) and the *Coefficient of Drag* (C_D), which are described by

$$C_L = C_L(\alpha, \delta_j), \tag{19}$$

$$C_D = C_{D_0} + \frac{C_L^2}{\pi \mathcal{A} \mathcal{R} e}, \tag{20}$$

where $\alpha = \arctan(w/u)$ is the surface's angle of attack[1], δ_j is the actuator deflection, C_{D_0} is the parasitic Coefficient of

[1]For the vertical stabilizer the sideslip angle $\beta = \arcsin(v/\|\mathbf{v}_B\|)$ is used instead of the angle of attack

Drag, $\mathcal{R}$ is the aspect ratio and e is the Oswald's efficiency. The Coefficient of Lift is given by

$$C_L = \begin{cases} C_{L_\alpha}\alpha + C_{L_{\delta_j}}\delta_j, & \text{if } -C_{L_{max}} \leq C_L \leq C_{L_{max}} \\ 0, & \text{otherwise} \end{cases}. \tag{21}$$

C_L is lower bounded at $-C_{L_{max}}$ and upper bounded at $C_{L_{max}}$. These limits induce loss of lift (stall) at angles of attack such that $\alpha \notin [\underline{\alpha}, \bar{\alpha}]$ where $C_L(\bar{\alpha}) = C_{L_{max}}$ and $C_L(\underline{\alpha}) = -C_{L_{max}}$. Applying (17) and (18) to the wing, horizontal stabilizer and vertical stabilizer one computes the Lift and Drag forces acting on the aircraft body L_w, D_w, L_{hs}, D_{hs}, L_{vs} and D_{vs}. Thus, the aerodynamic forces acting on the aircraft are given by (22) under the small angle approximation.

$$\mathbf{f}_a = \begin{bmatrix} D_w + D_{hs} + D_{vs} \\ L_{vs} \\ L_w + L_{hs} \end{bmatrix} \tag{22}$$

The aerodynamic moment $\mathbf{m}_a$ calculation requires the estimation of the aileron's mean pressure center location ($\mathbf{r}_a$), its slipstream mean pressure center ($\mathbf{r}_{p,a}$) location, the horizontal stabilizer's aerodynamic center location ($\mathbf{r}_{hs}$), the wing's aerodynamic center location ($\mathbf{r}_w$) and the vertical stabilizer's aerodynamic center location ($\mathbf{r}_{vs}$). Given these parameters it is then computed by

$$\mathbf{m}_a = \mathbf{m}_w + \mathbf{m}_{hs} + \mathbf{m}_{vs} + \begin{bmatrix} M_a \\ M_{damp_q} \\ M_{damp_r} \end{bmatrix}, \tag{23}$$

where M_a, $\mathbf{m}_{hs}$, $\mathbf{m}_{vs}$, $\mathbf{m}_w$, M_{damp_q} and M_{damp_r} define the aileron moment, the elevator moment, the rudder moment, the wing moment and the damping moments due to pitch and yaw rotation, respectively. The previously defined forces and moments complete the dynamic model description. The next section formulates the UAV Hybrid Automaton which accounts for controller switching during operating mode transitions.

III. Hybrid Automaton

The system's discrete behavior is captured by means of a Hybrid Automaton which is identified by: a set of the Operating Modes $\mathcal{Q}$; a Domain Mapping $\mathcal{D} : \mathcal{Q} \rightrightarrows \mathbb{R}^n \times \mathbb{R}^m$; a Flow Map $f : \mathcal{Q} \times \mathcal{D} \to \mathbb{R}^n$; a set of Edges $\mathcal{E} \subset \mathcal{Q} \times \mathcal{Q}$; a Guard Mapping $\mathcal{G} : \mathcal{E} \rightrightarrows \mathbb{R}^n \times \mathbb{R}^m$ and; a Reset Map $\mathcal{R} : \mathcal{E} \times \mathbb{R}^n \times \mathbb{R}^m \to \mathbb{R}^n$ (see [8] or [6] for further details). The system state $\boldsymbol{\xi} \in \mathbb{R}^{14}$ is defined in (1) and the actuator input $\boldsymbol{\mu} \in \mathbb{R}^7$ is given by

$$\mu = [\tau_1 \ \tau_2 \ \delta_a \ \delta_e \ \delta_r \ \delta_f \ q^*]^T, \tag{24}$$

where a new input variable $q^* \in \mathcal{Q}^* = \{H, L\}$ to inform the controller which is the desired Operating Mode and whether transition is required. The remaining state and input variables were defined in Section II.The Hybrid Automaton representation is provided in Figure 2.

A. Operating Modes

The Hybrid Automata operating mode q must belong to the set $\mathcal{Q} = \{H, X, L\}$ which has the meaning

- H - Hover operating mode with Hover controller selected, i.e. $\boldsymbol{\mu} = \boldsymbol{\mu}_H(\boldsymbol{\xi}, \boldsymbol{\xi}^*(t))$;
- X - Transition operating mode with Transition controller selected, i.e. $\boldsymbol{\mu} = \boldsymbol{\mu}_X(\boldsymbol{\xi}, \boldsymbol{\xi}^*(t))$;
- L - Level operating mode with Level controller selected, i.e. $\boldsymbol{\mu} = \boldsymbol{\mu}_L(\boldsymbol{\xi}, \boldsymbol{\xi}^*(t))$;

The variable $\boldsymbol{\xi}^\star(t)$ represents the reference state trajectory which the controller is tracking.

B. Domain Mapping

For each Operating Mode, the domain mapping $\mathcal{D} : \mathcal{Q} \rightrightarrows \mathbb{R}^{14} \times \mathbb{R}^6 \times \mathcal{Q}^*$ assigns the set where the variables $(\boldsymbol{\xi}, \boldsymbol{\mu})$ may range and it is defined by[2]

$$\begin{aligned} \mathcal{D}(H) =& [n_{min}, n_{max}]^2 \times \mathbb{R}^6 \times B_{\bar{\phi}_H}(0) \times B_{\bar{\theta}_H}(0) \times \\ & B_{\bar{\psi}_H}(0) \times \mathbb{R}^2 \times \mathbb{R}_{\leq 0} \times U \\ \mathcal{D}(X) =& [n_{min}, n_{max}]^2 \times \mathbb{R}_{\geq 0} \times \mathbb{R}^5 \times B_{\bar{\phi}_X}(0) \times B_{\bar{\theta}_X}(0) \times \\ & B_{\bar{\psi}_X}(0) \times \mathbb{R}^2 \times \mathbb{R}_{<0} \times U \\ \mathcal{D}(L) =& [n_{min}, n_{max}]^2 \times \mathbb{R}_{>0} \times \mathbb{R}^5 \times B_{\bar{\phi}_L}(0) \times B_{\bar{\theta}_L}(0) \times \\ & B_{\bar{\psi}_L}(0) \times \mathbb{R}^2 \times \mathbb{R}_{<0} \times U \bigcap \\ & \{(u, w) \in \mathbb{R}_{>0} \times \mathbb{R} : \underline{\alpha} < \arctan(w/u) < \bar{\alpha}\} \end{aligned} \tag{25}$$

where the actuators domain is the set $U \subset \mathbb{R}^3 \times \mathcal{Q}^*$ given by

$$\begin{aligned} U =& [\tau_{min}, \tau_{max}]^2 \times [\delta_{a_{min}}, \delta_{a_{max}}] \times [\delta_{e_{min}}, \delta_{e_{max}}] \times \\ & [\delta_{r_{min}}, \delta_{r_{max}}] \times [\delta_{f_{min}}, \delta_{f_{max}}] \times \mathcal{Q}^* \end{aligned} \tag{26}$$

The angle limits $\bar{\phi}_H$, $\bar{\phi}_L$, $\bar{\theta}_H$, $\bar{\theta}_L$, $\bar{\psi}_H$ and $\bar{\psi}_L$ are required for the Hover and Level Operating Modes domains to lie within the corresponding basin of attraction, i.e. if $\mathcal{B}_q$ is the basin of attraction for the operating mode q then $\mathcal{D}(q) \subset \mathcal{B}_q$.

C. Flow Map

The Flow Map $f : \mathcal{Q} \times \mathbb{R}^{14} \times U \to \mathbb{R}^6$ describes the evolution of the state variables in each operating mode $q \in \mathcal{Q}$, i.e. in each operating mode the state's derivative is given by

$$\dot{\boldsymbol{\xi}} = f(q, \boldsymbol{\xi}, \boldsymbol{\mu}_q) \tag{27}$$

where function f is the set of differential equations which describe the aircraft dynamic model.

D. Edges

The set of edges $\mathcal{E} \subset \mathcal{Q} \times \mathcal{Q}$ identifies any operating mode transition from q_1 to q_2 represented in Figure 2 with the pair (q_1, q_2). The possible operating mode transitions in this model are: (H, X), (X, L), (L, X) and (X, H).

[2] $B_\epsilon(p)$ represents a ball of radius ϵ around the point p, i.e. the set of points x such that $\|x - p\| < \epsilon$.

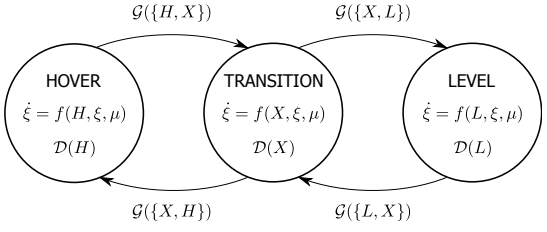

Fig. 2: The UAV Hybrid Automaton

E. Guard Mapping

The Guard Mapping $\mathcal{G} : \mathcal{E} \rightrightarrows \mathbb{R}^{14} \times \mathbb{R}^6 \times \mathcal{Q}^*$ determines for each pair (q_1, q_2) the set to which the aircraft state must belong in order to perform the transition. The switch from Hover to the Transition operating mode is performed only if the aircraft state verifies the controller restrictions on the initial state which are denoted by $\chi_{H\to X}$. Therefore, given a Transition to Level approach trajectory

$$v^{\star}_{X\to L}(t) = (\xi^{\star}_{X\to L}(t), \mu^{\star}_{X\to L}(t)),$$

switching from Hover to Transition occurs when the aircraft state is $\chi_{H\to X}$-close to $v^{\star}_{X\to L}(0)$. The guard mapping is similarly defined for the switch from Level to Transition.

Switching from Transition to either Hover or Level operating modes is performed whenever the aircraft state belongs to some set

$$X_q \subset \mathcal{D}(q) \tag{28}$$

where $q \in \{H, L\}$. Under the previous considerations, the Guard Mapping is defined by

$$\begin{aligned}
\mathcal{G}(H,X) =& B_{\chi_{H\to X}}(v^{*}_{X\to L}(0)) \\
\mathcal{G}(X,L) =& \Big\{(\boldsymbol{\xi},\boldsymbol{\mu}) \in \mathcal{D}(L) : |\phi| \le \bar{\phi}_{X\to L} \wedge \\
& |\theta| \le \bar{\theta}_{X\to L} \wedge |\psi| \le \bar{\psi}_{X\to L} \wedge q^* = L\Big\} \\
\mathcal{G}(L,X) =& B_{\chi_{L\to X}}(v^{*}_{X\to H}(0)) \\
\mathcal{G}(X,H) =& \Big\{(\boldsymbol{\xi},\boldsymbol{\mu}) \in \mathcal{D}(L) : |\phi| \le \bar{\phi}_{X\to H} \wedge \\
& |\theta| \le \bar{\theta}_{X\to H} \wedge |\psi| \le \bar{\psi}_{X\to H} \wedge q^* = H\Big\}
\end{aligned} \tag{29}$$

where the pitch angle boundaries $\bar{\phi}_{X\to L}$, $\bar{\theta}_{X\to L}$, $\bar{\psi}_{X\to L}$, $\bar{\phi}_{X\to H}$, $\bar{\theta}_{X\to H}$ and $\bar{\psi}_{X\to L}$ must verify

$$\begin{array}{lll}
\bar{\phi}_{X\to L} < \bar{\phi}_L & \bar{\theta}_{X\to L} < \bar{\theta}_L & \bar{\psi}_{X\to L} < \bar{\psi}_L \\
\bar{\phi}_{X\to H} < \bar{\phi}_H & \bar{\theta}_{X\to H} < \bar{\theta}_H & \bar{\psi}_{X\to H} < \bar{\psi}_H
\end{array}$$

in order to meet the condition (28). A guard mapping representation is given in Figure 3.

F. Reset Map

For each $(q_1, q_2) \in \mathcal{E}$ and $(\xi, \mu) \in \mathcal{G}(q_1, q_2)$, the reset map $\mathcal{R} : \mathcal{E} \times \mathbb{R}^{14} \times U \to \mathbb{R}^{14}$ identifies the jump of the state variable ξ during the operating mode transition from q_1 to q_2. State changes occur when switching from Transition to Level due to different attitude parametrization between the operating modes. The reset map is given by

$$\begin{aligned}
\mathcal{R}(H,X) =& \boldsymbol{\xi}, \\
\mathcal{R}(X,L) =& [n_1\ n_2\ u\ v\ w\ p\ q\ r\ \arctan({}^{B}_{N}\mathbf{R}_{23}/{}^{B}_{N}\mathbf{R}_{33}) \\
& \arcsin(-{}^{B}_{N}\mathbf{R}_{13})\ \arctan({}^{B}_{N}\mathbf{R}_{12}/{}^{B}_{N}\mathbf{R}_{11})\ x\ y\ z]^T, \\
\mathcal{R}(L,X) =& [n_1\ n_2\ u\ v\ w\ p\ q\ r\ \arctan({}^{B}_{U}\mathbf{R}_{23}/{}^{B}_{U}\mathbf{R}_{33}) \\
& \arcsin(-{}^{B}_{U}\mathbf{R}_{13})\ \arctan({}^{B}_{U}\mathbf{R}_{12}/{}^{B}_{U}\mathbf{R}_{11})\ x\ y\ z]^T, \\
\mathcal{R}(X,H) =& \boldsymbol{\xi},
\end{aligned} \tag{30}$$

where the symbol $\mathbf{R}_{ij}$ is the matrix $\mathbf{R}$ element which is found at the i-th row and j-th column.

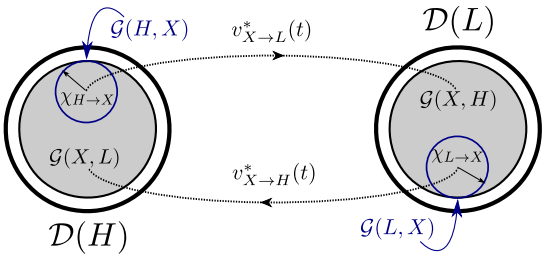

Fig. 3: Guard mapping representation

IV. Linear Quadratic Regulator

A. Controller Structure

The LQR control structure has already been extensively studied and is categorized as very reliable, for it has high gain and phase margins [12]. This control solution requires the system to be linear, however it has been proved that stabilization of a nonlinear system is also feasible within a neighborhood of the equilibrium point [13]. Classic LQR techniques provide the full state feedback control law $\tilde{\boldsymbol{\mu}} = -\mathbf{K}\tilde{\boldsymbol{\xi}}$ which robustly stabilizes the aircraft within a sublevel set of the Lyapunov function $V\tilde{\xi}) = \tilde{\xi}^T\tilde{\xi}$ near the linearization point $(\boldsymbol{\xi}_0, \boldsymbol{\mu}_0)$, where $\tilde{\boldsymbol{\xi}} = \boldsymbol{\xi} - \boldsymbol{\xi}_0$ and $\tilde{\boldsymbol{\mu}} = \boldsymbol{\mu} - \boldsymbol{\mu}_0$.

Each operating mode has a different operating point and specifications which require distinct weightings. Therefore controller dimensioning requires:

1) Linearization around the chosen operating point $(\boldsymbol{\xi}_q, \boldsymbol{\mu}_q)$;
2) Integrator states $(\bar{\boldsymbol{\xi}})$ choice according to the operating mode requirements;
3) Controllability evaluation;
4) $(\mathbf{Q}, \mathbf{R})$ weighting using Bryson's trial-and-error method, which employs the diagonal matrices

$$\mathbf{Q} = \begin{bmatrix} \Delta\boldsymbol{\xi}^{-2}_{1_{max}} & \cdots & 0 \\ \vdots & \ddots & \vdots \\ 0 & \cdots & \Delta\boldsymbol{\xi}^{-2}_{n_{max}} \end{bmatrix}, \tag{31}$$

$$\mathbf{R} = \begin{bmatrix} \Delta\boldsymbol{\mu}^{-2}_{1_{max}} & \cdots & 0 \\ \vdots & \ddots & \vdots \\ 0 & \cdots & \Delta\boldsymbol{\mu}^{-2}_{m_{max}} \end{bmatrix}, \tag{32}$$

where $\Delta\boldsymbol{\xi}_{i_{max}}$ represents the i-th state maximum expected deviation from equilibrium and $\Delta\boldsymbol{\mu}_{j_{max}}$ represents the j-th input maximum expected deviation from equilibrium.

The chosen control structure is that of D-methodology which is presented in Figure 4 which has several advantages over the classic LQR structure, including: it does not require the equilibrium point to be known, controller gains changes due to mode switching do not instantaneously change the actuator input and it provides anti-windup to the control if integrator output saturates whenever the actuators limits are reached.

B. Reference Maneuvers

The reference transition trajectories were generated with some intuitive insight about the system and considering that the transition is to occur in the vertical plane, *i.e.* the aircraft

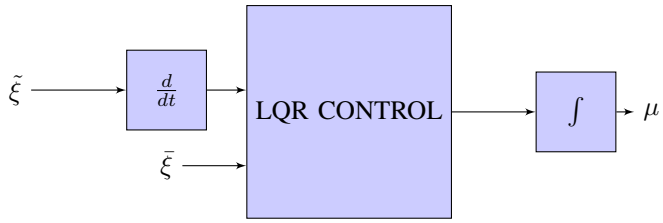

Fig. 4: D-methodology control structure.

is laterally stabilized. Therefore, the triplet (u^*, w^*, θ^*) fully defines the aircraft state at any given point. It is desirable that the reference trajectories do not lead the aircraft to a stall situation as it can be hazardous.

Considering firstly the transition from hover to level flight and assuming that the aircraft is able to climb up at a speed equal to that of level flight then the change in pitch angle is not troublesome, requiring solely the change of the main lifting force from thrust to wing lift. Under this assumption, the trajectories become very simple as the transition can be achieved with a step in the forward velocity u and a step in the pitch rate q. A ramp which takes the downward velocity w from the equilibrium value in hover to the equilibrium in level flight is considered instead of a step input in order to prevent stall during the transition.

The transition trajectory from level flight to hover is symmetric to the previous trajectory. The aircraft keeps its forward velocity while increasing steadily its pitch angle. Again, a ramp which takes the downward velocity from its equilibrium value in level flight to equilibrium in hover is considered as the reference trajectory.

C. Simulation Results

This section is divided into three different subsections which present the simulation results and numerical analysis performed in each individual operating mode. The nonlinear model presented in Section II was used given the parameter estimation which was performed on the real world model-scale UAV depicted in Figure 1a. Due to space constraints, the transition from Level to Hover is not presented for its similarity to the transition from Hover to Level.

D. Hover

The chosen operating point for the Hover controller dimensioning is given by

$$\begin{aligned}\boldsymbol{\xi}_{H_0} &\simeq [154.7\ 154.7\ 0\ 0\ 0\ 0\ 0\ 0\ 0\ \pi/2\ 0\ 0\ 0\ \ -1]^T,\\ \boldsymbol{\mu}_{H_0} &\simeq [0.12\ 0.12\ 0\ 0\ 0\ 0]^T.\end{aligned} \tag{33}$$

The controller structure introduced in Section IV is employed with

$$\begin{aligned}\tilde{\boldsymbol{\xi}}_H &= [n_1\ n_2\ u-u^*(t)\ v\ w-w^*(t)\ p\ q-q^*(t)\ r\ \phi\ \theta-\theta^*(t)\ \psi]^T\\ \bar{\boldsymbol{\xi}}_H &= [u-u^*(t)\ v\ w-w^*(t)\ \phi\ \theta-\theta^*\ \psi]^T.\end{aligned} \tag{34}$$

This particular choice of integrator states provides reference tracking (u^*, w^*, θ^*) and the required position stabilization when $(u^*, w^*, \theta^*) = (0, 0, 0)$. The trial-and-error method provides the weighting: $\Delta n_1 = \Delta n_2 = 200$ rps, $\Delta\tilde{u} = 10$ m/s, $\Delta\tilde{v} = \Delta\tilde{w} = 1$ m/s, $\Delta p = \Delta r = 1$ rad/s, $\Delta\tilde{q} = 0.1$ rad/s, $\Delta\tau_1 = \Delta\tau_2 = 0.2$ N.m, $\Delta\delta_a = \Delta\delta_f = 7.5°$ and $\Delta\delta_e = \Delta\delta_r = 15°$. Hover control simulations demonstrate the controller's ability to stabilize the aircraft at the operating point (33) starting from any initial condition which lies within Hover domain, $\boldsymbol{\xi}(0) \in \mathcal{D}(H)$, namely with initial conditions $\psi(0) = \bar{\psi}_H$ and $\theta(0) = \bar{\theta}_H$. Simulations results with the aforementioned starting angular values are depicted in Figure 5.

E. Level

The chosen operating point for the Level controller dimensioning is given by

$$\begin{aligned}\boldsymbol{\xi}_{L_0} &\simeq [112.4\ 112.4\ 10.8\ 0\ 1.9\ 0\ 0\ 0\ 0\ \pi/18\ 0\ \ -1]^T,\\ \boldsymbol{\mu}_{H_0} &\simeq [0.052\ 0.052\ 0\ \ -0.065\ 0\ 0]^T.\end{aligned} \tag{35}$$

The controller structure introduced in Section IV is employed with

$$\begin{aligned}\tilde{\boldsymbol{\xi}}_L &= [n_1\ n_2\ u-u^*(t)\ v\ w\ p\ q-q^*(t)\ r\ \phi\ \theta-\theta^*(t)\ \psi\ z]^T,\\ \bar{\boldsymbol{\xi}}_L &= [u-u^*(t)\ v\ \phi\ \theta-\theta^*(t)\ \psi]^T.\end{aligned} \tag{36}$$

The integrator states in the $\tilde{u}$ and $\tilde{\theta}$ stabilize the forward velocity and the pitch angle at some desired value. The state variable z stabilizes the aircraft at a given height. The trial-and-error method provides the weighting: $\Delta n_1 = \Delta n_2 = 200$ rps, $\Delta\tilde{u} = 10$ m/s, $\Delta\tilde{v} = \Delta\tilde{w} = 1$ m/s, $\Delta p = \Delta r = 1$ rad/s, $\Delta\tilde{q} = 0.1$ rad/s, $\Delta z = 0.1$ m, $\Delta\tau_1 = \Delta\tau_2 = 0.2$ N.m, $\Delta\delta_a = \Delta\delta_f = 7.5°$ and $\Delta\delta_e = \Delta\delta_r = 15°$. Level flight control must stabilize the aircraft at the equilibrium point in equation (35) as long as its initial state lies within the Level Flight domain, $\boldsymbol{\xi}(0) \in \mathcal{D}(L)$, namely with initial angles $\phi(0) = \bar{\phi}_L$ and $\theta(0) = \bar{\theta}_L$. Simulations results with the aforementioned starting angular values are depicted in Figure 6.

F. Transition

The transition flight does not have an equilibrium point in the same sense as level flight and hover but linearization around some equilibrium point is required in order to obtain

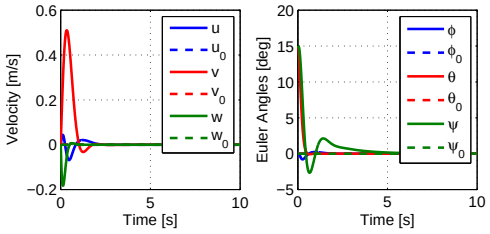

Fig. 5: Hover simulation - Velocity and Euler Angles time evolution.

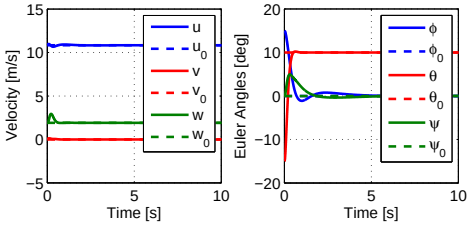

Fig. 6: Level simulation - Velocity and Euler Angles time evolution.

the Transition controller. The chosen operating point given in (37) is very similar to the Hover operating point. However, its forward velocity of 1 m/s provides the linear model with characteristics which are present both in hover and level flight.

$$\begin{aligned}\boldsymbol{\xi}_{X_0} &\simeq [157.3\ 157.3\ 1\ 0\ 0\ 0\ 0\ 0\ 0\ \pi/2\ 0\ 0\ 0\ \ -1]^T \\ \boldsymbol{\mu}_{X_0} &\simeq [0.12\ 0.12\ 0\ 0\ 0\ 0]^T\end{aligned} \tag{37}$$

Again, the controller structure described in Section IV is employed with

$$\begin{aligned}\tilde{\boldsymbol{\xi}}_X &= [n_1\ n_2\ u - u^*(t)\ v\ w - w^*(t)\ p\ q - q^*(t)\ r\ \phi\ \theta - \theta^*(t)\ \psi]^T \\ \bar{\boldsymbol{\xi}}_X &= [u - u^*(t)\ v\ w - w^*(t)\ \phi\ \theta - \theta^*\ \psi]^T,\end{aligned} \tag{38}$$

which is equal to the choice made for the Hover controller. However, the transition flight controller spans a large set of operating points which are defined by the reference maneuvers thus requiring different LQR weightings. The chosen weightings are $\Delta n_1 = \Delta n_2 = 200$ rps, $\Delta\tilde{u} = \Delta\tilde{v} = \Delta\tilde{w} = 10$ m/s, $\Delta p = \Delta r = \Delta\tilde{q} = 1$ rad/s, $\Delta\tau_1 = \Delta\tau_2 = 0.2$ N.m, $\Delta\delta_a = \Delta\delta_f = 7.5°$, $\Delta\delta_e = 15°$ and $\Delta\delta_r = 45°$. Simulation results show that the controller is able to stabilize the aircraft for the whole flight envelope. However, this feature comes at the cost of a more loosen reference tracking than that which is provided during hover and level flight.

1) Transition: Hover to Level: The aircraft starts its transition to level flight at the Hover equilibrium point and, since the reference transition trajectory starts at $u = 1\ m/s$, a step input with the same magnitude is required when in Hover. Figure 7 depicts the reference trajectory tracking and Figure 8 depicts the actuator inputs. The aircraft starts in Hover, switches to Transition at time $t = 0.9$ s when the aircraft state enters the guard map $\mathcal{D}(H, X)$ and switches to Level at $t = 9.6$ s when the guard map $\mathcal{D}(X, L)$ is breached. Nonlinear behavior is highly noticeable during switching from Hover to Transition due to input torque saturation. The lateral variables are not presented because the deviations from the vertical plane (x, z) are negligible.

V. Nonlinear Control

Despite the linear control solution feasibility, nonlinear control techniques are also exploited. However, due to its inherent complexity, model simplification is performed in Section V-A before the controller design provided in Section V-C. The nonlinear controller is tested within the simulation environment against the full aircraft model.The results are presented in V-D.

A. Simplified Model

The following simplifications are applied to the aircraft model presented in Section II:

- Propellers' dynamics are neglected. The thrust they provide is given by $T = \frac{T_1+T_2}{2}$;
- Lateral motion is stabilized which in turn implies that $T_1 - T_2$, δ_a, δ_r, v, p, r and y are null;
- The stall angle does not depend on the actuator deflection but only on the angle of attack which must verify $|\alpha| < \bar{\alpha}$, where $\bar{\alpha} = 15\,°$;
- The horizontal and vertical stabilizers drag as well as the flap contribution to the wing drag are neglected.

Under the previous assumptions, the configuration of the body frame $\{B\}$ with respect to $\{N\}$ can be viewed as an element of the Special Euclidean group, $(\mathbf{R}, \mathbf{p}) = ({}^N_B\mathbf{R}, {}^N\mathbf{p}_B) \in \mathrm{SE}(2)$ where

$${}^N\mathbf{p}_B = [x\ z]^T, \quad {}^N_B\mathbf{R} = \begin{bmatrix} \cos\theta & \sin\theta \\ -\sin\theta\cos\theta & \end{bmatrix}, \tag{39}$$

thus eliminating the singularity in the rotation matrix parametrization which occurs in three-dimensional rotations. The kinematics are described by

$${}^N\dot{\mathbf{p}}_B = {}^N_B\mathbf{R}\mathbf{v}_B, \quad \dot{\theta} = q, \tag{40}$$

where ${}^N\mathbf{p}_B = [x\ z]^T$ and $\mathbf{v}_B = [u\ w]^T$. Under the previous considerations, the main forces acting on the aircraft body are the wing lift L_w, the horizontal stabilizer lift L_{hs} and the wing drag D_w. The lifting forces L_{hs} and L_w produce the moments M_{hs} and M_w, respectively, due to their displacement with respect to the center of gravity. The moment M_{damp_q} remains valid in this analysis. The actuators input variables δ_e and δ_f can be changed into forces L_e and L_f, respectively, according to (41) and (42).

$$\delta_e = -\frac{L_e}{\frac{1}{2}\rho(2u_p^2)A_{p,hs}C_{L_{\delta_{e_{p,hs}}}} + \frac{1}{2}\rho u^2 A_{hs}C_{L_{\delta_{e_{hs}}}}} \tag{41}$$

$$\delta_f = -\frac{L_f}{\frac{1}{2}\rho(2u_p^2)A_{p,w}C_{L_{\delta_{f_{p,w}}}} + \frac{1}{2}\rho u^2 A_w C_{L_{\delta_{f_w}}}} \tag{42}$$

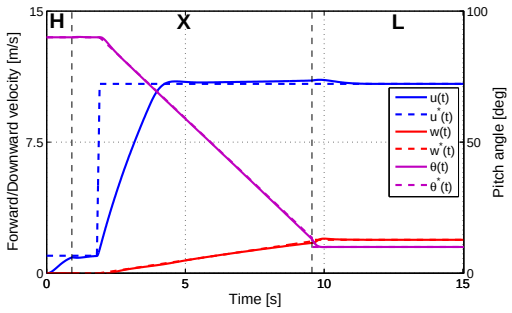

Fig. 7: Transition from Hover to Level simulation - reference tracking.

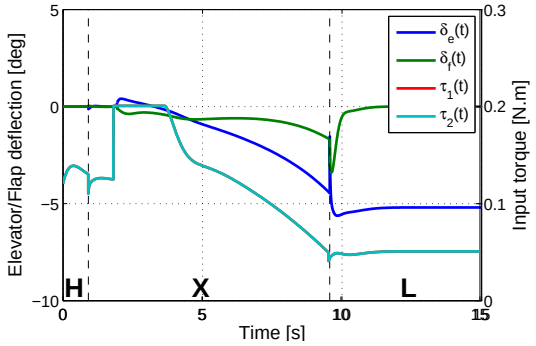

Fig. 8: Transition from Hover to Level simulation - actuator inputs.

The dynamics equations are rewritten in (43) for the longitudinal case, under the aforementioned simplifications.

$$\begin{aligned}\dot{u} &= \frac{2T}{m} + h_u(u, w, q, \theta),\\ \dot{w} &= \frac{L_f + L_e}{m} + h_w(u, w, q, \theta),\\ \dot{q} &= -\frac{\mathbf{r}_w.\,\mathbf{i}_B L_f + \mathbf{r}_{hs}.\,\mathbf{i}_B L_e}{\mathbf{I}_y} + h_q(u, w, q),\\ \dot{\theta} &= q.\end{aligned} \tag{43}$$

The new state variable to be monitored is

$$\boldsymbol{\xi} = [u\ w\ q\ \theta\ x\ z]^T,$$

thus, the Hybrid Automaton described in Section III is required to change in order to meet the specified simplifications.

B. Robust Maneuvers

The problem of achieving robust transitions between hover and level flights is twofold: *i)* the reference maneuver which links the two sets must be at least ϵ-distant from the domain limits and any guard sets leading to undesired operative mode transitions; *ii)* the controller must be able to achieve practical reference trajectory tracking with an error no larger than ϵ, in the presence of external disturbances and uncertain parameters.

Three different kinds of robust maneuvers are defined within the Hybrid Automata framework.The first one, which is denoted as ϵ-robust q_1-single maneuver in $[t_0, t_1)$, is such that the state and the input do not intersect any guard condition in order to maintain the same "single" operating mode q_1. The second type, denoted as ϵ-robust $q_1 \rightarrow q_2$ approach maneuver in $[t_0, T]$, is such that at time T the maneuver belongs robustly to the desired guard set, $\mathcal{G}(\{q_1, q_2\})$, in order to switch to the operating mode q_2. The last one, the $q_1 \rightarrow q_2$ transition maneuver in $[t_0, t_1)$, is obtained as a combination of an ϵ-robust $q_1 \rightarrow q_2$ approach maneuver and a set of ϵ-robust q_2-single maneuvers.

Although q_1-single maneuvers and $q_1 \rightarrow q_2$ transition maneuvers are defined for the hybrid automaton presented in Section III, the most important maneuvers are the $X \rightarrow L$ and $X \rightarrow H$ approach maneuvers which are identified by $v^\star_{X\rightarrow L}(t)$ and $v^\star_{X\rightarrow H}(t)$, respectively. These reference maneuvers are computed by means of system inversion. Given twice differentiable desired state trajectories $u^\star(t)$ and $\theta^\star(t)$, the downward velocity initial state $w^\star(0)$ and considering the flaps nominally at rest, i.e. $L^\star_f(t) = 0$ for all $t \geq 0$, then the reference control inputs $T^\star(t)$ and $L^\star_e(t)$, and the reference state variable $w^\star(t)$ are computed numerically by solving (43).

C. Controller Design

The controller design comprises two different methods: linear optimal control techniques are used when in Hover or Level operating modes, providing local stabilization; nonlinear control is used to perform the transition between the two disjoint operating modes.

In order to build the nonlinear controller and prove the overall system stability and robustness the state equations are rewritten in a simpler form by substituting the relations

$$\begin{bmatrix} L \\ M \end{bmatrix} = \begin{bmatrix} 1 & 1 \\ -\mathbf{r}_{hs}.\,\mathbf{i}_B & -\mathbf{r}_w.\,\mathbf{i}_B \end{bmatrix} \begin{bmatrix} L_e \\ L_f \end{bmatrix} \tag{44}$$

into (43). This substitution effectively rescales the control input throughout the maneuver. The new control input is described by

$$\boldsymbol{\mu} = \begin{bmatrix} T^\star(t) + \tilde{T} \\ M^\star(t) + \tilde{M} \\ L^\star(t) + \tilde{L} \end{bmatrix}, \quad \begin{aligned} \tilde{T} &= -k_u \tilde{u} \\ \tilde{M} &= -k_\theta(\tilde{\theta} + k_q \tilde{q}), \\ \tilde{L} &= -k_w \tilde{w} \end{aligned} \tag{45}$$

where $T^\star(t)$, $M^\star(t)$ and $L^\star(t)$ are the reference inputs obtained by model inversion as explained in Section V-B and $\tilde{T}$, $\tilde{M}$ and $\tilde{L}$ are the errors which result from practical reference tracking. Proportional-derivative (PD) controllers are used to track the reference trajectories. Substituting (45) into the system state equations (43), the aircraft error dynamics are described by

$$\dot{\tilde{u}} = \frac{2\tilde{T}}{m} + \Psi_u(\tilde{u}, \tilde{w}, \tilde{q}, \tilde{\theta}, t) + \delta_u(t), \tag{46a}$$

$$\dot{\tilde{w}} = \frac{\tilde{L}}{m} + \Psi_w(\tilde{u}, \tilde{w}, \tilde{q}, \tilde{\theta}, t) + \delta_w(t), \tag{46b}$$

$$\dot{\tilde{q}} = \frac{\tilde{M}}{\mathbf{I}_y} + \Psi_q(\tilde{u}, \tilde{w}, \tilde{q}, t) + \delta_q(t), \tag{46c}$$

$$\dot{\tilde{\theta}} = q, \tag{46d}$$

where the functions Ψ_u, Ψ_w and Ψ_q described by (47) have been introduced and the perturbation terms $\delta_u(t)$, $\delta_w(t)$ and $\delta_q(t)$ have been added. These perturbations may appear due to parametric uncertainty, external disturbances and/or due to deviations from the vertical plane.

$$\begin{aligned}\Psi_u(\tilde{u}, \tilde{w}, \tilde{q}, \tilde{\theta}, t) =& h_u(u^\star(t) + \tilde{u}, w^\star(t) + \tilde{w}, q^\star(t) + \tilde{q}, \theta + \tilde{\theta}) \\ &- h_u(u^\star(t), w^\star(t), q^\star(t), \theta^\star(t))\\ \Psi_w(\tilde{u}, \tilde{w}, \tilde{q}, \tilde{\theta}, t) =& h_w(u^\star(t) + \tilde{u}, w^\star(t) + \tilde{w}, q^\star(t) + \tilde{q}, \theta + \tilde{\theta}) \\ &- h_w(u^\star(t), w^\star(t), q^\star(t), \theta^\star(t))\\ \Psi_q(\tilde{u}, \tilde{w}, \tilde{q}, t) =& h_q(u^\star(t) + \tilde{u}, w^\star(t) + \tilde{w}, q^\star(t) + \tilde{q}) \\ &- h_q(u^\star(t), w^\star(t), q^\star(t))\end{aligned} \tag{47}$$

The reference trajectory is one of equilibrium (if $\delta_u = \delta_w = \delta_q = 0$) because

$$[\tilde{u}\ \tilde{w}\ \tilde{q}\ \tilde{\theta}] = [0\ 0\ 0\ 0] \Rightarrow [\dot{\tilde{u}}\ \dot{\tilde{w}}\ \dot{\tilde{q}}\ \dot{\tilde{\theta}}] = [0\ 0\ 0\ 0].$$

The previous set of equations provides the foundations upon which the nonlinear controller's robustness emerges. Consider two separate but interconnected systems which describe the pairs $(\tilde{u}, \tilde{w})$ and (θ_1, θ_2), where $\theta_1 = \tilde{\theta}$ and $\theta_2 = \tilde{q} + \frac{\tilde{\theta}}{k_q}$. Input-to-State Stability is proven firstly for each of these system separately in Propositions 1 and 2. Input-to-State Stability for the overall system then follows from the Small Gain Theorem described in both [14] and [15], which is applied to the feedback interconnection depicted in Figure 9.

Proposition 1: For some $c^\star_u > 0$ and $c^\star_w > 0$ and any numbers satisfying $\Delta > 0$, $\overline{\|(\theta_1, \theta_2)\|} > 0$, $0 < c_u < c^\star_u$ and $0 < c_w < c^\star_w$ there exist $k_u > k^\star_u$ and $k_w > k^\star_w$ such that the system with the dynamics (46a) and (46b) is rendered ISS with restrictions c_u in the initial state $\tilde{u}(0)$, c_w on the initial state $\tilde{w}(0)$, Δ on the inputs $\delta_u(t)$ and $\delta_w(t)$ and $\overline{\|(\theta_1, \theta_2)\|}$ on the input $(\theta_1(t), \theta_2(t))$.

Proof: Consider the Lyapunov function (48) and the level set definition given in (49).

$$V_1(\tilde{u},\tilde{w}) = \frac{1}{2}(\tilde{u}^2+\tilde{w}^2) \tag{48}$$

$$\Omega_1(l) = \{(\tilde{u},\tilde{w}) \in \mathbb{R}^2 : V_1(\tilde{u},\tilde{w}) \leq l\} \tag{49}$$

$$\tag{50}$$

It turns out that, due to radial unboundedness there exist positive l_1 such that

$$\{(\tilde{u},\tilde{w}) \in \mathbb{R}^2 : |\tilde{u}| \leq c_u \wedge |\tilde{w}| \leq c_w\} \subset \Omega_1(l_1). \tag{51}$$

Moreover, for any given reference trajectory it is possible to find $c_u^\star$, $c_w^\star$ and $l_1^\star$ such that

$$\{(\tilde{u},\tilde{w}) \in \mathbb{R}^2 : |\tilde{u}| \leq c_u^\star \wedge |\tilde{w}| \leq c_w^\star\} \subset \Omega_1(l_1^\star), \tag{52}$$

and

$$\left\{(\tilde{u},\tilde{w}) \in \Omega_1(l_1^\star) : u^\star(t)+\tilde{u} > 0 \wedge \left|\arctan\left(\frac{w^\star(t)+\tilde{w}}{u^\star(t)+\tilde{u}}\right)\right| < \bar{\alpha}\right\}, \tag{53}$$

hold true for all $t \geq 0$.

The functions defined in (47) are locally Lipschitz because the functions h_u, h_w and h_q are continuous and proper, therefore there exist positive L_u and L_w such that for all $(\tilde{u},\tilde{w}) \in \Omega_1(l_1)$ and $\|(\theta_1(t),\theta_2(t))\| < \overline{\|(\theta_1,\theta_2)\|}$ the following holds

$$\left\|\Psi_u\left(\tilde{u},\tilde{w},\theta_2-\frac{\theta_1}{k_q},\theta_1,t\right)\right\| \leq L_u\|(\tilde{u},\tilde{w},\theta_1,\theta_2,t)\|, \tag{54}$$

$$\left\|\Psi_w\left(\tilde{u},\tilde{w},\theta_2-\frac{\theta_1}{k_q},\theta_1,t\right)\right\| \leq L_w\|(\tilde{u},\tilde{w},\theta_1,\theta_2,t)\|, \tag{55}$$

for all $t \geq 0$. The Lyapunov function derivative $\dot{V}_1$ is given by

$$\begin{aligned}\dot{V}_1 = \tilde{u}\left(-\frac{2k_u}{m}\tilde{u}+\Psi_u\left(\tilde{u},\tilde{w},\theta_2-\frac{\theta_1}{k_q},\theta_1,t\right)+\delta_u(t)\right)\\ +\tilde{w}\left(-\frac{k_w}{m}\tilde{w}+\Psi_w\left(\tilde{u},\tilde{w},\theta_2-\frac{\theta_1}{k_q},\theta_1,t\right)+\delta_w(t)\right).\end{aligned} \tag{56}$$

Substituting (54) and (55) into (56) and using the triangle inequality, the Lyapunov function's derivative can be upper bounded by

$$\begin{aligned}\dot{V}_1 \leq &-\lambda_{min}\|(\tilde{u},\tilde{w})\|^2+\|(\tilde{u},\tilde{w})\|((L_u+L_w)\|(\theta_1,\theta_2)\|+\\ &+\delta_u(t)+\delta_w(t)),\end{aligned} \tag{57}$$

where λ_{min} is the smallest eigenvalue of the matrix

$$\begin{bmatrix}\frac{2k_u}{m}+L_u & \pm\frac{1}{2}(L_u+L_w)\\ \pm\frac{1}{2}(L_u+L_w) & \frac{k_w}{m}+L_w\end{bmatrix}.$$

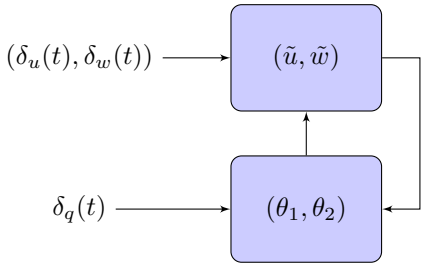

Fig. 9: Interconnected systems $(\tilde{u},\tilde{w})$ and (θ_1,θ_2).

It is easy to verify that for any $\Delta > 0$ and $\overline{\|(\theta_1,\theta_2)\|} > 0$ there exist $k_w^\star > 0$ and $k_u^\star(k_w^\star) > 0$ such that for any $k_u > k_u^\star$, $k_w > k_w^\star$, $(\delta_u(t),\delta_w(t))$ satisfying $\|\delta_u(t)\|_\infty \leq \Delta$, $\|\delta_w(t)\|_\infty \leq \Delta$, and $\|(\theta_1(t),\theta_2(t))\|_\infty < \overline{\|(\theta_1,\theta_2)\|}$ and for any $(\tilde{u},\tilde{w}) \in \Omega_1(l_1)$ the following holds

$$\dot{V}_1 < 0 \text{ if } \|(\tilde{u},\tilde{w})\| > \frac{L_u+L_w}{\lambda_{min}}\|(\theta_1(t),\theta_2(t))\|+\frac{\delta_u(t)+\delta_w(t)}{\lambda_{min}}. \tag{58}$$

The system has a local ISS function, therefore it is ISS with restrictions c_u on the initial state $\tilde{u}(0)$, c_w on the initial state $\tilde{w}(0)$ and Δ on the inputs $\delta_u(t)$ and $\delta_w(t)$ as long as the conditions $c_u < c_u^\star$ and $c_w < c_w^\star$ are satisfied.

■

Proposition 2 employs similar arguments to those in Proposition 1 proof in order to justify the Input-to-State Stability of the closed-loop system (θ_1,θ_2).

Proposition 2: For any arbitrary positive numbers Δ, $\overline{\|\tilde{u},\tilde{w}\|}$, k_q, c_q and c_θ there exists $k_\theta^\star(k_q) > 0$ such that $k_\theta > k_\theta^\star$ renders the system with the dynamics (46a) and (46b) ISS with restrictions c_q on the initial state $\tilde{q}(0)$, c_θ on the initial state $\tilde{\theta}(0)$, $\overline{\|\tilde{u},\tilde{w}\|}$ on the input $(\tilde{u}(t),\tilde{w}(t))$ and Δ on the input $\delta_q(t)$.

Proof: Consider the Lyapunov function described by (59) and the level set definition given in (60).

$$V_2(\theta_1,\theta_2) = \frac{1}{2}(\theta_1^2+\theta_2^2) \tag{59}$$

$$\Omega_2(l) = \{(\theta_1,\theta_2) \in \mathbb{R}^2 : V_2(\theta_1,\theta_2) \leq l\} \tag{60}$$

Due to radial unboundedness there exists positive l_2 such that

$$\left\{(\theta_1,\theta_2) \in \mathbb{R}^2 : |\theta_1| \leq c_\theta \wedge \left|\theta_2-\frac{\theta_1}{k_q}\right| \leq c_q\right\} \subset \Omega_2(l_2). \tag{61}$$

The function Ψ_q is continuous and proper in $\Omega_2(l_2)$, therefore there exists positive L_q such that for all $(\theta_1,\theta_2) \in \Omega_2(l_2)$, $\|\tilde{u}(t),\tilde{w}(t)\| < \overline{\|\tilde{u},\tilde{w}\|}$ the following holds

$$\left\|\Psi_q\left(\tilde{u},\tilde{w},\theta_2-\frac{\theta_1}{k_q},t\right)\right\| \leq L_q\|(\tilde{u},\tilde{w},\theta_1,\theta_2,t)\|, \tag{62}$$

for all $t \geq 0$. The Lyapunov function derivative $\dot{V}_2$ is given by

$$\begin{aligned}\dot{V}_2 =&\theta_1\left(\theta_2-\frac{\theta_1}{k_q}\right)+\theta_2\left(-\frac{k_\theta k_q}{I}\theta_2+\right.\\ &\left.+\Psi_q\left(\tilde{u},\tilde{w},\theta_2-\frac{\theta_1}{k_q},t\right)+\frac{\theta_2}{k_q}-\frac{\theta_1}{k_q^2}\right),\end{aligned} \tag{63}$$

where the derivatives $\dot{\theta}_1$ and $\dot{\theta}_2$ are

$$\begin{aligned}\dot{\theta}_1 =&\theta_2-\frac{\theta_1}{K_q},\\ \dot{\theta}_2 =&-\frac{k_\theta k_q}{\mathbf{I}_y}\theta_2+\Psi_q\left(\tilde{u},\tilde{w},\theta_2-\frac{\theta_1}{k_q},t\right)+\frac{\theta_2}{k_q}-\frac{\theta_1}{k_q^2}.\end{aligned} \tag{64}$$

Let Ω be the set defined by

$$\Omega(\underline{l},\bar{l}) = \left\{(\theta_1,\theta_2) \in \mathbb{R}^2 : \underline{l} \leq \|(\theta_1,\theta_2)\| \leq \bar{l}\right\}, \tag{65}$$

and let $\bar{l} = l_2$ and choose a number $\underline{l} \in \mathbb{R}^+$ satisfying $0 < \underline{l} < \bar{l}$. The Lyapunov function derivative taken on the set $\Omega(\underline{l},\bar{l}) \cap \{(\theta_1,\theta_2) \in \mathbb{R}^2 : \theta_2 = 0\}$ is

$$\dot{V}_2 = -\frac{\theta_1^2}{k_q}, \tag{66}$$

verifying that $\dot{V}_2 < 0$. By continuity, the Lyapunov function derivative verifies this condition also in an open superset $\mathcal{M}$ of $\Omega(\underline{l}, \bar{l}) \cap \{(\theta_1, \theta_2) \in \mathbb{R}^2 : \theta_2 = 0\}$. Note that $\Omega(\underline{l}, \bar{l})/\mathcal{M}$ is compact and let

$$\underline{\theta}_2 = \min_{\theta_2 \in \Omega_2((\underline{l}),(\bar{l}))/\mathcal{M}} |\theta_2|,$$
$$\bar{\theta}_2 = \max_{\theta_2 \in \Omega_2((\underline{l}),(\bar{l}))/\mathcal{M}} |\theta_2| \text{ and}$$
$$\bar{\theta}_2 = \max_{\theta_1 \in \Omega_2(l_2)} |\theta_1|.$$

Making use of the previous definitions it is possible to find the upper bound of the Lyapunov function derivative given in (67).

$$\dot{V}_2 \leq -\left(\frac{k_\theta k_q}{\mathbf{I}_y}\underline{\theta_2} - \left(\frac{1}{k_q} + L_q\right)\bar{\theta_2} - \left(1 + \frac{1}{k_q^2} + L_q\right)\bar{\theta_1} - \right.$$
$$\left. - L_q\overline{\|(\tilde{u}, \tilde{w})\|} - \Delta\right)|\theta_2| - \frac{\theta_1^2}{k_q} \tag{67}$$

It is easy to see that for any $\Delta > 0$ and $\overline{\|(\tilde{u}, \tilde{w})\|} > 0$ there exists a suitable choice of $k_\theta^\star(k_q) > 0$ such that for $k_\theta > k_\theta^\star$, $\tilde{u}$, $\tilde{w}$ and $\delta_q(t)$ satisfying $\|(\tilde{u}(t), \tilde{w}(t))\|_\infty < \overline{\|(\tilde{u}, \tilde{w})\|}$ and $|\delta_q(t)| < \Delta$ the Lyapunov function's derivative verifies $\dot{V}_2 < 0$ for any (θ_1, θ_2) belonging to $\Omega_2(\underline{l}, \bar{l})$.

The system has a local ISS Lyapunov function therefore it is ISS with restrictions c_θ on the initial state $\tilde{\theta}(0)$, c_q on the initial state $\tilde{q}(0)$, $\overline{\|(\tilde{u}, \tilde{w})\|}$ on the input $(\tilde{u}, \tilde{w})$ and Δ on the input $\delta_q(t)$. ■

Notice that the restrictions on the inputs of the interconnected systems

$$\|(\tilde{u}(t), \tilde{w}(t))\|_\infty < \overline{\|(\tilde{u}, \tilde{w})\|},\ \|(\theta_1(t), \theta_2(t))\|_\infty < \overline{\|(\theta_1, \theta_2)\|}$$

are satisfied by taking

$$\overline{\|(\tilde{u}, \tilde{w})\|} = \max_{(\tilde{u}, \tilde{w}) \in \Omega_1(l_1)} \|(\tilde{u}, \tilde{w})\|$$

and

$$\overline{\|(\theta_1, \theta_2)\|} = \max_{(\theta_1, \theta_2) \in \Omega_2(l_2)} \|(\theta_1, \theta_2)\|.$$

Under the previous definitions and results, the input-to-state stability for the overall system is established in Proposition 3.

Proposition 3: For some $c_u^\star > 0$ and $c_w^\star > 0$ and any numbers satisfying $\Delta > 0$, $0 < c_u < c_u^\star$, $0 < c_w < c_w^\star$, $k_q > 0$, $c_q > 0$ and $c_\theta > 0$ there exist $k_u^\star > 0$, $k_w^\star > 0$ and $k_\theta^\star(k_q) > 0$ such that the system with dynamics (46) is rendered ISS with restrictions c_u on the initial state $\tilde{u}(0)$, c_w on the initial state $\tilde{w}(0)$, c_q on the initial state $\tilde{q}(0)$, c_θ on the initial state $\tilde{\theta}(0)$ and Δ on the inputs $\delta_u(t)$, $\delta_w(t)$ and $\delta_q(t)$.

Proof: Input-to-state stability with restrictions for the individual systems $(\tilde{u}, \tilde{w})$ and (θ_1, θ_2) is proved in Propositions 1 and 2, respectively. The small gain theorem requires that the condition

$$k_1 k_2 < 1$$

is met, where k_1 is the closed-loop system $(\tilde{u}, \tilde{w})$ asymptotic gain relative to the input (θ_1, θ_2) and, similarly, k_2 is the closed-loop system (θ_1, θ_2) asymptotic gain relative to the input $(\tilde{u}, \tilde{w})$. The asymptotic gain k_1 decreases with increasing k_u or k_w and k_2 can be fixed arbitrarily with an appropriate choice of k_θ, therefore, the small gain theorem condition is met. Moreover, the tracking error can be made arbitrarily small. ■

Proposition 3 concludes the stability and robustness analysis. We have proven that a transition trajectory can be tracked with an arbitrary small error. This allows for the use of the Hybrid Automata framework to achieve stability of the overall hybrid system. The next section presents simulation results which makes use of the open-source hybrid systems simulator presented in [16].

D. Simulation Results

The simulations were performed using the open-source tool provided in [16] employing the hybrid automaton equivalence to the generic hybrid system which is given in [6].

The chosen reference trajectories for the transition maneuvers are described by

$$u^\star(t) = \begin{cases} u_0, & \text{if } t_0 \leq t < t_u \\ u_0 + (u_\infty - u_0)\exp(-\Phi_u(t - t_u)). & \\ \quad (\exp(\Phi_u(t - t_u)) - \Phi_u(t - t_u) - 1), & \text{if } t \geq t_u \end{cases} \tag{68}$$

$$\theta^\star(t) = \begin{cases} \theta_0 & \text{if } t_0 \leq t < t_\theta \\ \theta_0 + (\theta_\infty - \theta_0)\exp(-\Phi_\theta(t - t_\theta)) & \\ \quad (\exp(\Phi_\theta(t - t_\theta)) - \Phi_\theta(t - t_\theta) - 1), & \text{if } t \geq t_\theta \end{cases} \tag{69}$$

which are characterized by the initial forward velocity u_0, the final forward velocity u_∞, the initial pitch angle θ_0, the final pitch angle θ_∞, the transition start times t_θ and t_u and the parameters Φ_u and Φ_θ which determine the speed at which the transition is performed for each of the state variables u and θ, respectively. These trajectories were used for hover to level flight and level flight to hover transitions with appropriate parameter choice. Due to space constraints, only the hover to level flight transition maneuver is presented. This maneuver has the following parametric values: $u_0 = 1$ m/s, $u_\infty = 10.83$ m/s, $\Phi_u = 1$ s^{-1}, $t_u = 0$ s, $\theta_0 = 90°$, $\theta_\infty = 10°$, $\Phi_\theta = 0.7$ s^{-1} and $t_\theta = 0.1$ s. The input variable T must be transformed into the real input variables $\tau_{1,2}$. This task is accomplished using the relation

$$\tau = \frac{\rho d^5 C_P n^2}{2\pi} \tag{70}$$

where n is the propeller speed which provides the thrust $T = T^* + \tilde{T}$ and it is the solution of (8). This control input disregards the propeller's dynamic behavior and this imprecision adds to the perturbation terms δ_u, δ_w and δ_q which the control loop is able to handle. The simulations also require the definition of the controller restrictions on the initial states ($c_u = c_w = 0.1$ m/s, $c_q = 0.02$ rad/s and $c_\theta = 0.02$ rad) and on the controller gains ($k_u = k_w = 10$ N.s/m, $k_q = 1$ s and $k_\theta = 10$ N.s/m).

Figure 10 depicts the aircraft state variables flow with time and Figure 11. The aircraft starts in hover at $u = 0$ m/s and the local controller increases thrust in order to achieve a forward velocity of $u = 1$ m/s which is the transition maneuver starting point. When the aircraft state is near $v_{X \to H}^\star(0)$ a switch occurs (at $t \simeq 0.91$ s) and the nonlinear controller is used in order to follow the reference. Transition to level flight occurs when $\theta < \bar{\theta}_{X \to L}$ (at $t = 8.0$ s) and the local regulator stabilizes the aircraft at the equilibrium point.

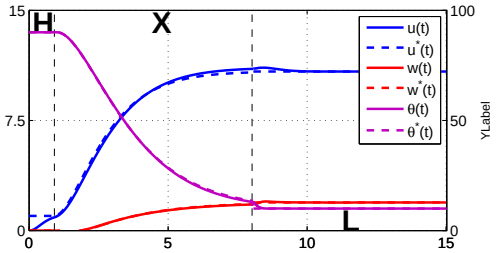

Fig. 10: Hover to Level transition - forward velocity, downward velocity and pitch angle flow with time

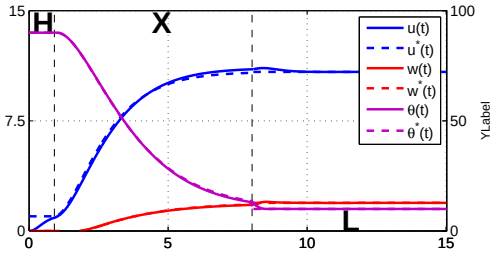

Fig. 11: Hover to Level transition - actuators input

VI. Conclusion

This paper presented an Unmanned Air Vehicle (UAV) model which described the aircraft dynamics during both hover and level flights. The main forces and moments affecting the aircraft dynamics can be divided into three different classes - gravity, propeller and aerodynamics - according to their nature. The aerodynamic forces and moments arise from the free-stream flow and the propeller slipstream which are computed separately and combined together in the end using superposition. An appropriate choice of the inertial and body-fixed coordinates frames was essential for kinematic modeling, where the Euler angles provided rotation parametrization. Moreover, this model also included the propeller dynamics, increasing the model's accuracy with respect to the model presented in [3]. The Hybrid Automata framework provided the means to handle controller switching between the three operating modes: Hover, Level and Transition.

Linear Optimal techniques successfully provided Hover and Level stabilization as well as reference tracking during the transition between these two operating modes. Furthermore, this solution proved to be robust with respect to parameters change. Similar solutions were employed in [4], [17], [18] and [5] and their success was only proved within a simulation environment. Successful real world transitions between hover and level flights are presented in [19], [3] and [20] which employ either open-loop or remotely operated maneuvers.

Therefore, Section V constitutes the most important contribution of this paper for it provides a formal proof of stability and robustness within a 2-dimensional aircraft model. The nonlinear controller designed in this chapter renders the system locally input-to-state stable with restriction on the disturbances inputs and initial state. Reference maneuvers design by means of model inversion combined with practical reference tracking provides robust transition between the two disjoint operating modes Hover and Level.

Simulation results proved that both linear and nonlinear control laws constitute a feasible solution to the transition problem. Future work relies on:

- Controller analysis in the presence of wind disturbances and sensor noise within the simulation environment;
- Transition trajectories optimization;
- Model verification and more accurate parameter estimation with real world testing which would create a reliable platform for controller design, verification and validation;
- Controller implementation at the given aircraft platform constitutes also the basis for future work.

References

[1] T. Samad, J. Bay, and D. Godbole. Network-centric systems for military operations in urban terrain: The role of uavs. In *Proceedings of the IEEE*, 2007.

[2] K. Ro, J. S. Oh, and L. Dong. Lessons learned: Application of small uav for urban highway traffic monitoring. In *45th AIAA Aerospace Sciences Meeting and Exhibit*, 2007.

[3] Frank Adrian, James S. McGrew, Mario Valenti, Daniel Levine, and Jonathan P. How. Hover, transition, and level flight control design for a single-propeller indoor airplane. In *AIAA Guidance, Navigation and Control Conference*, 2007.

[4] Steven Cornelius Kriel. A comparison of control systems for the flight transition of vtol unmanned aerial vehicles. Master's thesis, University of Stellenbosch, 2008.

[5] Stephen R. Osborne. Transitions between hover and level flight for a tailsitter uav. Master's thesis, Brigham Young University, United States of America, 2007.

[6] Rafal Goebel, Ricardo G. Sanfelice, and Andrew R. Teel. Hybrid dynamical systems. *IEEE Control Systems Magazine*, 2009.

[7] Ricardo G. Sanfelice and Andrew R. Teel. A throw-and-catch hybrid control strategy for robust global stabilization of nonlinear system. In *American Control Conference*, 2007.

[8] L. Marconi, R. Naldi, and L. Gentili. A control framework for robust practical tracking of hybrid automata. In *Joint 48th IEEE Conference on Decision and Control and 28th Chinese Control Conference*, 2009.

[9] Daniel Liberzon and Stephen Morse. Basic problems in stability and design of switched systems. *IEEE Control Systems Magazine*, 1999.

[10] D. Cabecinhas, R. Naldi, L. Marconi, C. Silvestre, and R. Cunha. Robust take-off and landing for a quadrotor vehicle. In *IEEE Conference on Robotics and Automation*, 2010.

[11] Xenofon D. Koutsoukos, Panos J. Antsaklis, James A. Stiver, and Michael D. Lemmon. Supervisory control of hybrid systems. In *Proceedings of the IEEE*, 2000.

[12] Gene F. Franklin, J. David Powell, and Abbas Emami-Naeini. *Feedback Control of Dynamic Systems*. Addison-Wesley, 1994.

[13] Jean-Jacques E. Slotine and Weiping Li. *Applied Nonlinear Control*. Prentice Hall, 1991.

[14] Alberto Isidori, Lorenzo Marconi, and Andrea Serrani. *Robust Autonomous Guidance*. Springer, 2003.

[15] Hassan K. Khalil. *Nonlinear Systems*. Prentice Hall, 2002.

[16] Ricardo G. Sanfelice and Andrew R. Teel. Dynamical properties of hybrid systems simulators. *Automatica*, 46, 2009.

[17] R. Hugh Stone. *Modelling and control of mini-flying machines*, chapter 7. Springer, 2005.

[18] Nathan B. Knoebel. Adaptive quaternion control of a miniature tailsitter uav. Master's thesis, Brigham Young University, United States of America, 2007.

[19] William E. Green and Paul Y. Oh. A mav that flies like an airplane and hovers like a helicopter. In *Proceeding of the 2005 IEEE/ASME*, 2005.

[20] Alexis Lussier Desbiens, Alan Asbeck, and Mark Cutkosky. Hybrid aerial and scansorial robotics. In *IEEE Conference on Robotics and Automation*, 2010.